Letter

Compact spin-valley-locked perovskite emission

Yang Chen [1,9,11], Jiangang Feng [2,10,11] ✉, Yuqing Huang [2,3,11], Weijin Chen[1], Rui Su [2], Sanjib Ghosh [4], Yi Hou [5,6], Qihua Xiong [4,7,8] ✉ & Cheng-Wei Qiu [1] ✉

Circularly polarized light sources with free-space directional emission play a key role in chiroptics[1], spintronics[2], valleytronics[3] and asymmetric photocatalysis[4]. However, conventional approaches fail to simultaneously realize pure circular polarization, high directionality and large emission angles in a compact emitter. Metal-halide perovskite semiconductors are promising light emitters[5–8], but the absence of an intrinsic spin-locking mechanism results in poor emission chirality. Further, device integration has undermined the efficiency and directionality of perovskite chiral emitters. Here we realize compact spin-valley-locked perovskite emitting metasurfaces where spin-dependent geometric phases are imparted into bound states in the continuum via Brillouin zone folding, and thus, photons with different spins are selectively addressed to opposite valleys. Employing this approach, chiral purity of 0.91 and emission angle of 41.0° are simultaneously achieved, with a beam divergence angle of 1.6°. With this approach, we envisage the realization of chiral light-emitting diodes, as well as the on-chip generation of entangled photon pairs.

Circularly polarized light carrying spin angular momentum is essential for a plethora of applications such as chiral sensing[9], display technologies[10] and quantum computation[11]. However, ultracompact, ultrathin chiral light sources inevitably face considerable challenges in luminescence efficiency, emission directionality and chiral purity. Metal-halide perovskites appear to be promising materials for light-emitting devices due to their high luminescence quantum efficiency, tunable bandgap and solution processability[5–8], but in contrast to spintronic materials (for example, transition metal dichalcogenides and ferromagnets), they do not possess the spin degree of freedom in electronic structures and thus are not suitable for generating circularly polarized light. Although

perovskite emission can be made chiral via chiral ligands[12,13], the resulting chiral purity is very limited. The miniaturization of a perovskite emitter further degrades the efficiency and directionality of emission (Supplementary Section 1).

Recently, bound states in the continuum (BICs), as peculiar topological states that decouple from far-field radiation and lying within the light cone, have been exploited for metasurface-assisted emission owing to their high quality (Q) factors[14–26]. Since the topological configuration of BIC usually exhibits a polarization vortex centred at the Γ point of the Brillouin Zone (BZ), the resulting BIC emission is mostly limited to vortex beams radiated around the normal direction[15–19]. A few

[1]Department of Electrical and Computer Engineering, National University of Singapore, Singapore, Singapore. [2]Division of Physics and Applied Physics, School of Physical and Mathematical Sciences, Nanyang Technological University, Singapore, Singapore. [3]Department of Physics, Chemistry and Biology (IFM), Linköping University, Linköping, Sweden. [4]Beijing Academy of Quantum Information Sciences, Beijing, People's Republic of China. [5]Department of Chemical and Biomolecular Engineering, National University of Singapore, Singapore, Singapore. [6]Solar Energy Research Institute of Singapore (SERIS), National University of Singapore, Singapore, Singapore. [7]State Key Laboratory of Low-Dimensional Quantum Physics and Department of Physics, Tsinghua University, Beijing, People's Republic of China. [8]Frontier Science Center for Quantum Information, Beijing, People's Republic of China. [9]Present address: Chinese Academy of Sciences Key Laboratory of Mechanical Behavior and Design of Materials, Department of Precision Machinery and Precision Instrumentation, University of Science and Technology of China, Hefei, People's Republic of China. [10]Present address: Department of Electrical and Computer Engineering, National University of Singapore, Singapore, Singapore. [11]These authors contributed equally: Yang Chen, Jiangang Feng, Yuqing Huang. ✉e-mail: jiangang.feng@ntu.edu.sg; qihua_xiong@tsinghua.edu.cn; chengwei.qiu@nus.edu.sg
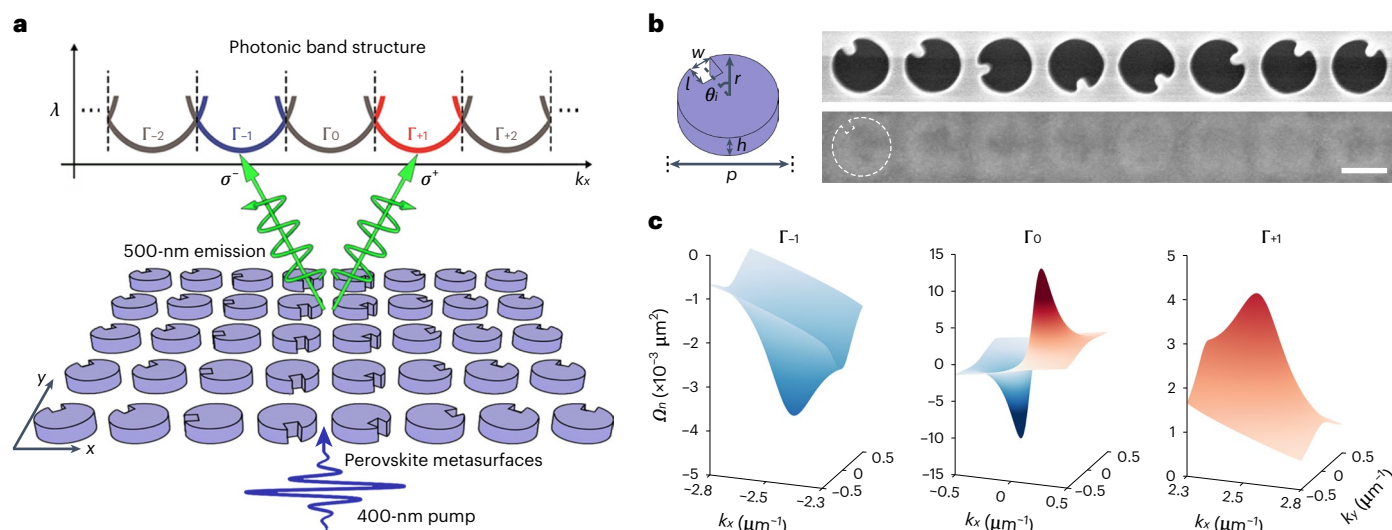
Fig. 1 | Spin-valley-locked emission in perovskite metasurfaces. a, Schematic of the perovskite metasurface enabling spin-valley-locked emission. The Γ_{-1} (Γ_{+1}) valley, formed by BZ folding, is selectively addressed by emitted photons with σ^- (σ^+) polarization. The units are rotated with an angle sequence of 35°, 46°, 100°, 197°, 228°, 293°, 326°, 329° from left to right. **b,** SEM images of the silica template (top) and perovskite metasurface (bottom), where only one period is shown.

The geometric parameters are $p = 316$ nm, $r = 125$ nm, $h = 160$ nm, $l = 60$ nm and $w = 50$ nm. The contour of the perovskite metasurface is blurred because of the conformal growth of perovskites inside the silica nanoholes. Perovskite and silica have similar contrast in the SEM images. Scale bar, 200 nm. **c,** Modified form of Berry curvature Ω_n calculated in the Γ_{-1}, Γ_0 and Γ_{+1} valleys.

BIC attempts have achieved chiral photoluminescence (PL) by generating a pair of circularly polarized states in the vicinity of the Γ point via structural perturbations[22–24], but the two emission lobes produced with opposite helicities are still near the normal direction and thus spatially mixed in the far field due to their poor directionality. As to the chiral emission approach based on chiral BICs[27,28], three-dimensional chiral geometry with a specific slant angle is critical for enabling high-purity chiral emission. A small deviation of the slant angle could cause the breakdown of the chiral BIC, which has put forward strict requirements on the utilized three-dimensional fabrication method and made this approach inextensible to other luminescent materials. Also, its emission direction is fixed to the normal direction. Besides, wide-angle directional emission has also been pursued based on diffractive leakage[20] or off-Γ BIC[21], but their achieved emission angles are limited (<28°) and they cannot have circular polarization.

We construct synthetic valleys in the photonic band structure of the BIC metasurface and endow the spin-valley-locking feature to perovskite emission. Formamidinium lead bromide (FAPbBr$_3$) perovskites are directly assembled into an ultracompact metasurface of a square array of perovskite nanocylinders with lattice constant p (Fig. 1a). We develop a self-limiting assembly method to allow the conformal growth of polycrystalline perovskites inside the metasurface template (Supplementary Section 2). The conformal growth of perovskites is guaranteed by the incorporation of phenylethylammonium bromide (PEABr), which can constrain the grain size in the crystallization process. This allows both well-defined photonic structures with a feature size down to 50 nm and the growth of high-quality perovskites with long-range homogeneity (Fig. 1b), which is reflected by bright and homogeneous luminescence in 40×40 μm^2 regions (Supplementary Fig. 4). The conformal growth and crystal structure of perovskites are characterized by cross-sectional scanning electron microscopy (SEM) images and X-ray diffraction, respectively (Supplementary Fig. 4).

If the nanocylinders have no notches, the photonic band structure of the TE$_{10}$ mode exhibits a local band extremum at the Γ point of the BZ, also termed as a Γ valley. A symmetry-protected BIC is achieved at the Γ valley due to the in-plane inversion ($C2$) symmetry (Supplementary Section 3). The nature of the weakly dispersive higher-frequency mode is also analysed in Supplementary Section 3. Furthermore, the

introduction of notches that cyclically rotate within a supercell of N units ($N = 8$ here) replicates the Γ valley by BZ folding (Supplementary Section 4), resulting in a series of synthetic valleys Γ_v (v is the valley index) in the extended BZs whose momenta are $(k_x, k_y) = (2\pi v/Np, 0)$ (Fig. 1a). The determination of structural parameters for the metasurface is discussed in Supplementary Section 5. Despite being mutually connected by translation symmetry, these Γ_v valleys exhibit different far-field emission properties and hence behave as inequivalent valleys in emission. Under optical pumping, photons emitted from the perovskites are coupled to the high-Q BIC mode and selectively addressed to opposite valleys (Γ_{+1} and Γ_{-1}) according to their different spins (Fig. 1a). Such spin-valley locking of emitted photons resembles that of excitons in transition metal dichalcogenides[29–31], where the valley-dependent Berry curvatures are manifested. Similar connection can also be found in our system by considering a modified form of the Berry curvature $\vec{\Omega}_n$ for a given band $|n\rangle$:

$$\vec{\Omega}_n \equiv -\mathrm{Im}\left[\sum_{v=0} \langle \nabla_{\vec{k}} n | \Psi_v \rangle \times \langle \Psi_v | \nabla_{\vec{k}} n \rangle \right]. \tag{1}$$

The summation only includes the Bloch state $|\Psi_v\rangle$ at $v = 0$ that is solely responsible for the emission (Supplementary Section 5). As defined, $\vec{\Omega}_n$ does not imply the topology of the eigenmode but serves as an effective magnetic field in the momentum space acting solely on the radiative photons[32]. Here $\Omega_{n,z}$, as the z component of $\vec{\Omega}_n$, is calculated to be opposite for Γ_{+1} and Γ_{-1} valleys to induce spin-valley locking (Fig. 1c).

The emission mechanism of the metasurface can be interpreted with a tight-binding model, involving the hopping and interaction of pseudospin-1 particles among the lattice sites (Supplementary Section 6). The local mode is characterized by pseudospin projections along the z axis[33–35], where $S_z = 0$ corresponds to a non-radiative monopole mode and $S_z = \pm 1$ correspond to the radiative dipole modes with $\sigma^\pm$-polarized far-field emission (Fig. 2a). The Hamiltonian of the system is derived as

$$\mathcal{H} = \mathcal{H}_0 + \mathcal{V}_{os} + \mathcal{V}_{nn}, \tag{2}$$

where $\mathcal{H}_0$ describes the metasurface without notches, giving rise to a gapped Dirac-like dispersion[34] at the vicinity of the Γ point
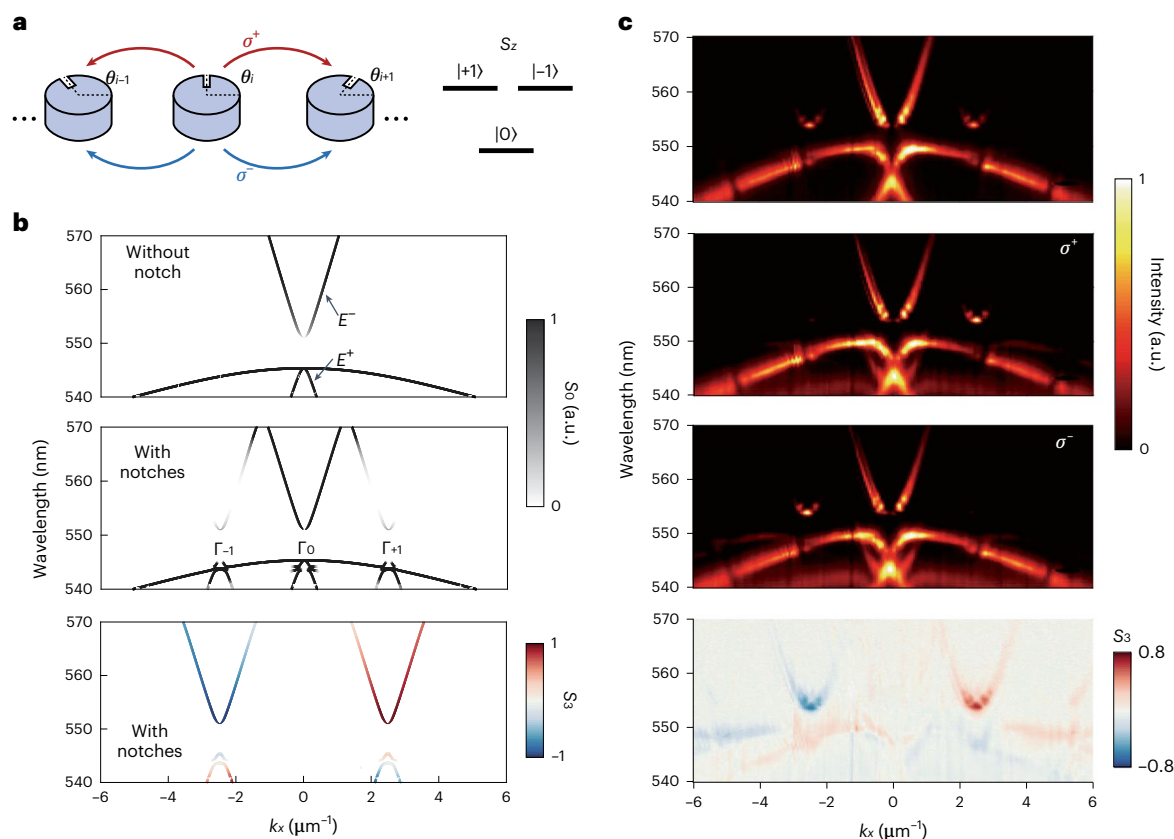
Fig. 2 | Spontaneous emission properties of perovskite metasurfaces.
a, Schematic of the tight-binding model with on-site and nearest-neighbour interactions. **b**, Theoretical dispersion of S_0 for the metasurface without (top) and with (middle) rotational notches. Dispersion of S_3 normalized by S_0 for the case with notches (bottom). **c**, Measured angle-resolved spectra of PL emission with linear, σ^+ and σ^- polarizations. Normalized S_3 is calculated as $S_3 = (I_{\sigma^+} - I_{\sigma^-})/(I_{\sigma^+} + I_{\sigma^-})$, where I_{σ^+} and I_{σ^-} are the intensities of σ^+ and σ^- emission, respectively.

(Fig. 2b). The eigenmode energies can be expanded with a small reciprocal vector $\vec{q}$ with respect to the Γ point as $E_0 = e_0$ and $E_\pm = e_0/2 \pm \sqrt{e_0^2 + 4\eta^2 |\vec{q}|^2}/2$. Here e_0 is the gap energy at the Γ point and η is the hopping strength related to spin–orbit coupling. The contribution of the dark mode $S_z = 0$ rises sharply as $\vec{q}$ approaches 0, leading to the at-Γ BIC for the typical dispersion of the TE$_{10}$ mode. Here $\mathcal{V}_{os}$ and $\mathcal{V}_{nn}$ are the on-site and the nearest-neighbour interaction terms, respectively, associated with the introduction of perturbative notches that wind for $\mathcal{W}$ times ($\mathcal{W} = 1$ here) within a supercell. Also, $\mathcal{W}$ is a positive/negative number for counterclockwise/clockwise winding. Specifically, $\mathcal{V}_{os} = \alpha \sum_{j} \sum_{m=\pm 1} \psi_j^{m\dagger} \psi_j^0 e^{-im\theta_j} + \psi_j^{0\dagger} \psi_j^m e^{im\theta_j}$ originates from the breaking of rotational symmetry of the nanocylinder due to the notches. Here θ_j denotes the rotational angle of the notch. Here $\psi_j^{m\dagger}$ and ψ_j^m are the creation and annihilation operator of the local modes at site j with a given spin quantum number m, respectively. Also, $\mathcal{V}_{os}$ couples the local mode of $S_z = 0$ and $S_z = \pm 1$. Such on-site spin mixing predominantly happens at $\Gamma_{\pm\mathcal{W}}$ to selectively brighten these two valleys. The emission right at Γ_0 is forbidden due to the restored C_2^z symmetry. The far-field emission intensity in terms of Stokes parameter S_0 at $\Gamma_{\pm\mathcal{W}}$ valleys reads

$$S_0 \left(\Gamma_{\pm\mathcal{W}} + \vec{q} \right) = \kappa^2 \left(1 - \varepsilon^2 |\vec{q}|^2 \right), \tag{3}$$

where $\kappa = \alpha/e_0$ and $\varepsilon = \eta/e_0$ indicate the effective strength of $\mathcal{V}_{os}$ and hopping strength in $\mathcal{H}_0$, respectively. Accordingly, the emission intensity is the strongest at the centre of the $\Gamma_{\pm\mathcal{W}}$ valley and rapidly drops when moving away from the centre (Fig. 2b). On the other hand, $\mathcal{V}_{nn} = \frac{\beta}{2} \sum_{\langle l,j \rangle} \left[e^{i(\theta_j - \phi_{j,l})} + e^{i(\theta_l - \phi_{l,j})} \right] \psi_l^{0\dagger} \psi_j^0 + $ h.c. originates from the perturbed hopping of the dark mode by the notches. Here $\phi_{j,l}$ denotes the hopping angle from site j to l. Also, $\mathcal{V}_{nn}$ vanishes when the rotation angle of the notch remains the same, for example, along the y axis. Hopping along the screw axis, for example, the x axis, is accompanied by a phase factor that is determined by both hopping direction $\phi_{j,l}$ and local rotational angle θ_j. The combined effect of $\mathcal{V}_{os}$ and $\mathcal{V}_{nn}$ is the accumulation of opposite geometric phases (GPs) as the state $S_z = +1$ and -1 hops along the screw axis. It builds up opposite phase gradients and scatters these two states into opposite valleys. Stokes parameter S_3 associated with the helicity of the emission at $\Gamma_{\pm\mathcal{W}}$ valleys reads

$$S_3 (\Gamma_{\pm\mathcal{W}}) = \pm \mathrm{sgn} [\mathcal{W}] \frac{\kappa\gamma}{\sqrt{4\varepsilon^2 \sin^2 (2\pi\mathcal{W}/N) + 1}}, \tag{4}$$

where $\gamma = \beta/\eta$ is the ratio of hopping strengths in $\mathcal{V}_{nn}$ and $\mathcal{H}_0$. Equation (4) precisely captures the spin-valley-locking phenomenon with normalized S_3 possessing large values of opposite signs in $\Gamma_{\pm\mathcal{W}}$ valleys (Fig. 2b). If the winding direction is reversed, that is, the sign of $\mathcal{W}$ is changed, it is naturally anticipated that the circular polarization in the $\Gamma_{\pm\mathcal{W}}$ valleys will be flipped.

To experimentally investigate the spontaneous emission performance of perovskite metasurfaces, we exploit angle-resolved PL spectroscopy under the excitation of a 455 nm continuous-wave laser with linear polarization (Methods). The measured dispersions (Fig. 2c) are in good agreement with the theoretical results.
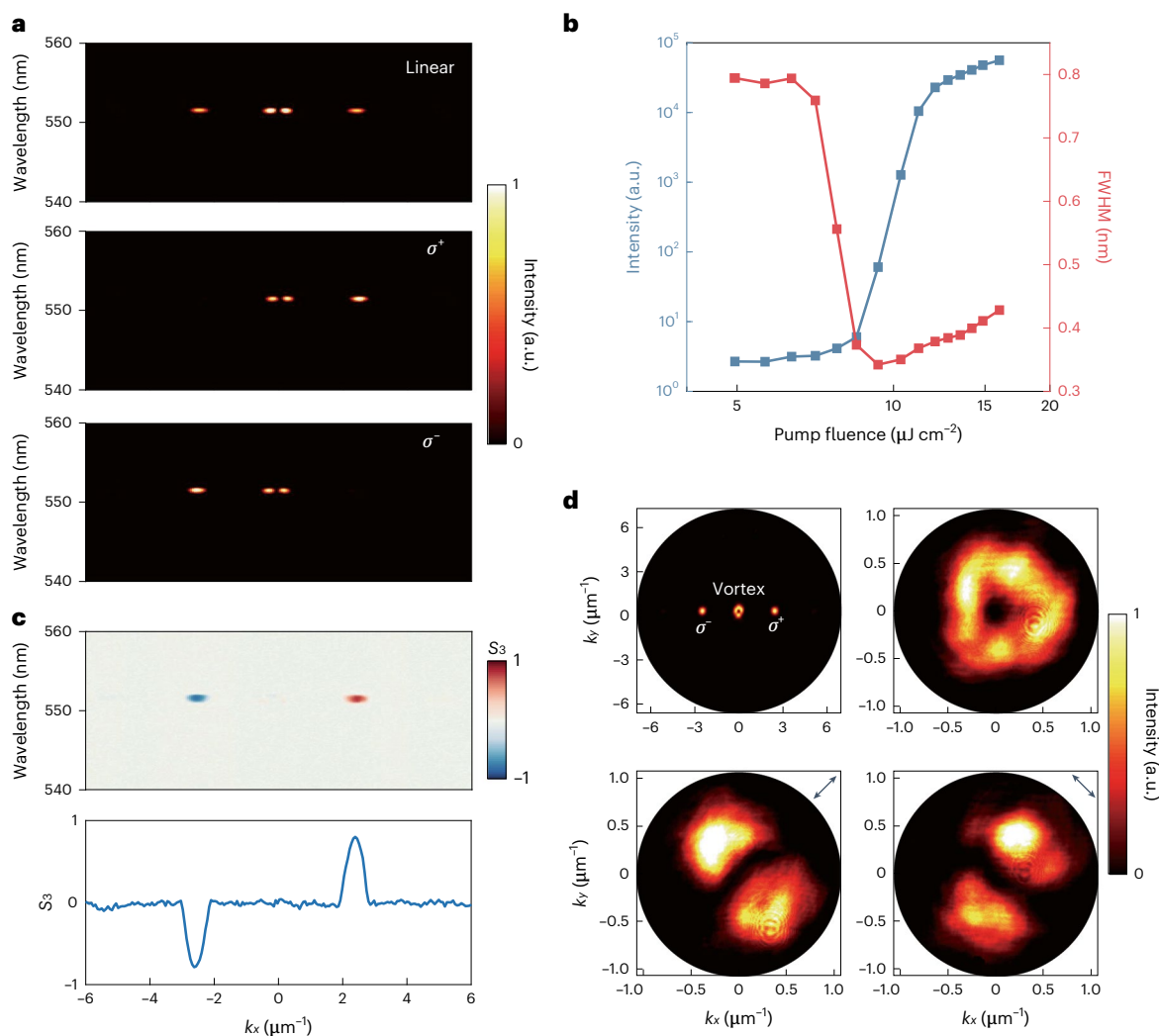
Fig. 3 | Spin-valley-locked lasing measured in perovskite metasurfaces.
a, Angle-resolved spectra of lasing with linear, σ^+ and σ^- polarizations measured above the threshold. **b**, Integrated intensity and full-width at half-maximum (FWHM) as a function of pump fluence. **c**, Retrieved dispersion of normalized S_3 (top) and a linecut at 553 nm (bottom). **d**, Momentum-space images of the lasing emission. The zoomed-in images illustrate an azimuthally polarized vortex laser at the Γ_0 valley.

The topmost continuous band represents the Γ_0 valley of the TE_{10} mode, within which the diminishing point at the bottom indicates the formation of BIC. Meanwhile, two isolated bright spots are clearly observed on both sides of the Γ_0 valley, corresponding to the Γ_{-1} (left) and Γ_{+1} (right) valley; their emission angles are −13° and +13°, respectively. By examining the polarization of PL, the Γ_{+1} and Γ_{-1} valleys predominantly possess σ^+ and σ^+ polarizations with normalized S_3 parameters up to +0.66 and −0.66, respectively (Fig. 2c), which are considerably larger than the existing works[12,13,23] (Supplementary Section 1). The Γ_0 valley is linearly polarized with negligible S_3. Owing to spin-valley locking, the isolated emission in Γ_{+1} and Γ_{-1} valleys simultaneously exhibits narrow widths of 0.5 μm^{-1} and 0.8 nm in momentum and spectrum, respectively, corresponding to a small beam divergence angle of 1.6° and Q factor of 700. Such narrow-k–narrow-λ PL emissions have been rarely demonstrated before. For comparison, we have presented the emission measurement results of perovskite metasurfaces with unrotated notches (Supplementary Section 7).

The high-Q BIC serves as a cavity mode for lasing. When the perovskite metasurface is excited by a 400 nm femtosecond laser with the pump fluence exceeding a threshold, the measured dispersion exhibits four lasing spots at 553 nm, all of which belong to the TE_{10} mode

(Fig. 3a), because it is the only cavity mode in the gain spectrum of the perovskite. The lasing action is explicitly demonstrated by the evolution of integrated intensity and linewidth with the pump fluence (Fig. 3b). Above a threshold of 8.5 $\mu J\,cm^{-2}$, the emission intensity experiences a pronounced rise, whereas the linewidth is narrowed from 0.80 to 0.34 nm, corresponding to a lasing Q factor of 1,600 (Supplementary Fig. 11). Although previously reported perovskite lasers have realized comparable threshold and Q factor, they cannot achieve both directional and circularly polarized emission[36–41].

Due to spin-valley locking, the lasing polarization is σ^+ and σ^- for the Γ_{+1} and Γ_{-1} valleys. The measured S_3 parameters, up to +0.8 and −0.8, are even higher than those of spontaneous emission for the enhancement in coherence (Fig. 3c). The two adjacent spots at the centre are attributed to the generation of a BIC vortex laser, as revealed by the intensity profiles mapped in momentum space (Fig. 3d). A doughnut-shaped beam with a central dark zone is observed. By placing a linear polarizer after the vortex beam, two lobes are present whose directions follow the axis of the linear polarizer, suggesting the azimuthal polarization distribution of the beam.

The emission property can be further tailored by rearranging the rotational angles inside a supercell to impart different GPs. When the winding constant w equals 2, the GP-carried lasing is expected to take
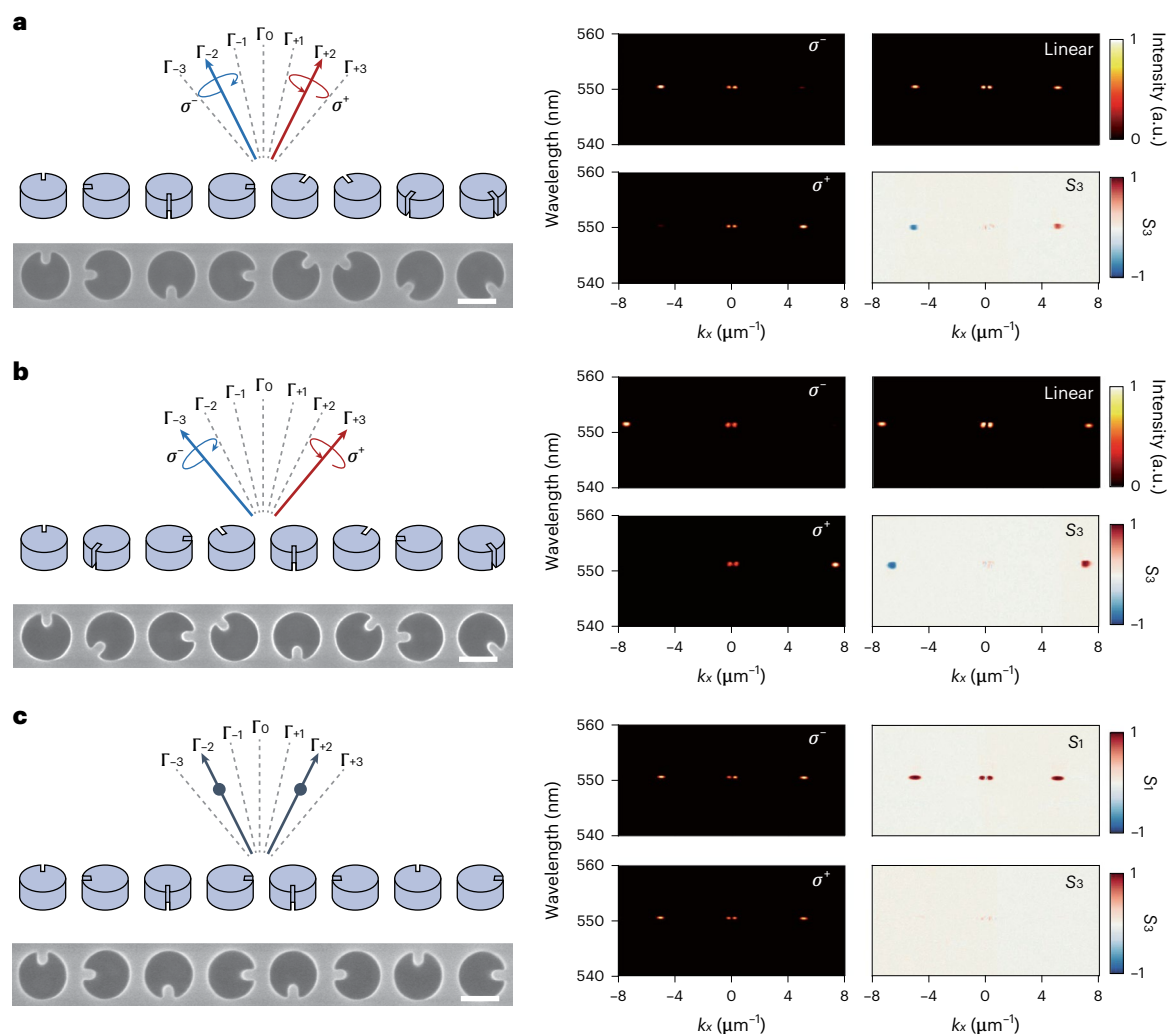
Fig. 4 | Perovskite lasing with tunable valleys and polarizations. a,b, Spin-valley-locked lasing at the $\Gamma_{\pm2}$ valleys for $\mathcal{W} = 2$ (**a**) and $\Gamma_{\pm3}$ valleys for $\mathcal{W} = 3$ (**b**). **c,** Linearly polarized lasing at the $\Gamma_{\pm2}$ valleys for $\mathcal{W} = 0$. Angle- and polarization-resolved lasing spectra, as well as the corresponding Stokes parameters (right). Scale bars (SEM images), 200 nm.

place at the Γ_{+2} and Γ_{-2} valleys to possess σ^+ and σ^- polarizations, respectively, which is experimentally validated (Fig. 4a). For the case of $\mathcal{W} = 3$ (Fig. 4b), the lasing valleys are switched to Γ_{+3} and Γ_{-3}, with the emission angles further increased to 41° and −41°, respectively. The achieved emission angles are much larger than previous works involving directional emission[20,21]. Besides, the corresponding normalized S_3 values of +0.91 and −0.91 are much higher than most of the existing chiral emission works[12,13,23,24]. Detailed experimental results are provided in Supplementary Fig. 12. Nevertheless, when it comes to the case of $\mathcal{W} = 0$, the accumulated GP over a supercell becomes trivial and thus spin-valley locking is released (Fig. 4c). Here the supercell can be decomposed into two halves: the left half generates beams of σ^+ and σ^- polarizations at the Γ_{+2} and Γ_{-2} valleys, respectively, whereas the right half with a reversed winding direction produces lasers at the same valleys but with opposite spins. The resulting lasers are, thus, linearly polarized. We note that spontaneous PL emission exhibits similar features of tunable valleys and polarizations (Supplementary Fig. 13).

Our results provide a distinct paradigm to modulate both coherent and incoherent emission processes, which could be widely applied to thermoluminescence, electroluminescence and spontaneous parametric downconversion. It poses no stringent requirements for luminescent materials and hence can be extended to other luminescent media, such as transition metal dichalcogenides, gallium arsenide

and quantum dots. In addition to spin-valley locking, more flexible functionalities can be anticipated by rearranging the unit cells of the metasurface, paving the way towards a plethora of applications in light sources and detectors, display technologies and quantum optics.

Online content

Any methods, additional references, Nature Portfolio reporting summaries, source data, extended data, supplementary information, acknowledgements, peer review information; details of author contributions and competing interests; and statements of data and code availability are available at https://doi.org/10.1038/s41563-023-01531-2.

References

1. Chen, Y. et al. Multidimensional nanoscopic chiroptics. *Nat. Rev. Phys.* **4**, 113–124 (2021).
2. Hirohata, A. et al. Review on spintronics: principles and device applications. *J. Magn. Magn. Mater.* **509**, 166711 (2020).
3. Schaibley, J. R. et al. Valleytronics in 2D materials. *Nat. Rev. Mater.* **1**, 16055 (2016).
4. Wang, L., Yin, L., Zhang, W., Zhu, X. & Fujiki, M. Circularly polarized light with sense and wavelengths to regulate azobenzene supramolecular chirality in optofluidic medium. *J. Am. Chem. Soc.* **139**, 13218–13226 (2017).

5. Sutherland, B. R. & Sargent, E. H. Perovskite photonic sources. *Nat. Photon.* **10**, 295–302 (2016).

6. Stranks, S. D. & Snaith, H. J. Metal-halide perovskites for photovoltaic and light-emitting devices. *Nat. Nanotechnol.* **10**, 391–402 (2015).

7. Luo, J. et al. Efficient and stable emission of warm-white light from lead-free halide double perovskites. *Nature* **563**, 541–545 (2018).

8. Kim, Y.-H. et al. Chiral-induced spin selectivity enables a room-temperature spin light-emitting diode. *Science* **371**, 1129–1133 (2021).

9. Hendry, E. et al. Ultrasensitive detection and characterization of biomolecules using superchiral fields. *Nat. Nanotechnol.* **5**, 783–787 (2010).

10. Zheng, G. et al. Metasurface holograms reaching 80% efficiency. *Nat. Nanotechnol.* **10**, 308–312 (2015).

11. Sherson, J. F. et al. Quantum teleportation between light and matter. *Nature* **443**, 557–560 (2006).

12. Long, G. et al. Spin control in reduced-dimensional chiral perovskites. *Nat. Photon.* **12**, 528–533 (2018).

13. Ma, J. et al. Chiral 2D perovskites with a high degree of circularly polarized photoluminescence. *ACS Nano* **13**, 3659–3665 (2019).

14. Hsu, C. W., Zhen, B., Stone, A. D., Joannopoulos, J. D. & Soljačić, M. Bound states in the continuum. *Nat. Rev. Mater.* **1**, 16048 (2016).

15. Kodigala, A. et al. Lasing action from photonic bound states in continuum. *Nature* **541**, 196–199 (2017).

16. Huang, C. et al. Ultrafast control of vortex microlasers. *Science* **367**, 1018–1021 (2020).

17. Wu, M. et al. Room-temperature lasing in colloidal nanoplatelets via Mie-resonant bound states in the continuum. *Nano Lett.* **20**, 6005–6011 (2020).

18. Hwang, M. S. et al. Ultralow-threshold laser using super-bound states in the continuum. *Nat. Commun.* **12**, 4135 (2021).

19. Tian, J. et al. Phase-change perovskite microlaser with tunable polarization vortex. *Adv. Mater.* **35**, 2207430 (2022).

20. Ha, S. T. et al. Directional lasing in resonant semiconductor nanoantenna arrays. *Nat. Nanotechnol.* **13**, 1042–1047 (2018).

21. Azzam, S. I. et al. Single and multi-mode directional lasing from arrays of dielectric nanoresonators. *Laser Photonics Rev.* **15**, 2000411 (2021).

22. Wang, J. et al. Routing valley exciton emission of a WS₂ monolayer via delocalized Bloch modes of in-plane inversion-symmetry-broken photonic crystal slabs. *Light. Sci. Appl.* **9**, 148 (2020).

23. Tian, J. et al. Optical Rashba effect in a light-emitting perovskite metasurface. *Adv. Mater.* **34**, 2109157 (2022).

24. Kim, S. et al. Topological control of 2D perovskite emission in the strong coupling regime. *Nano Lett.* **21**, 10076–10085 (2021).

25. Ardizzone, V. et al. Polariton Bose–Einstein condensate from a bound state in the continuum. *Nature* **605**, 447–452 (2022).

26. Reineke Matsudo, B. et al. Efficient frequency conversion with geometric phase control in optical metasurfaces. *Adv. Sci.* **9**, 2104508 (2022).

27. Zhang, X., Liu, Y., Han, J., Kivshar, Y. & Song, Q. Chiral emission from resonant metasurfaces. *Science* **377**, 1215–1218 (2022).

28. Chen, Y. et al. Observation of intrinsic chiral bound states in the continuum. *Nature* **613**, 474–478 (2023).

29. Mak, K. F., McGill, K. L., Park, J. & McEuen, P. L. The valley Hall effect in MoS₂ transistors. *Science* **344**, 1489–1492 (2014).

30. Wang, G. et al. Colloquium: excitons in atomically thin transition metal dichalcogenides. *Rev. Mod. Phys.* **90**, 021001 (2018).

31. Rivera, P. et al. Valley-polarized exciton dynamics in a 2D semiconductor heterostructure. *Science* **351**, 688–691 (2016).

32. Xiao, D., Chang, M.-C. & Niu, Q. Berry phase effects on electronic properties. *Rev. Mod. Phys.* **82**, 1959 (2010).

33. Fang, A., Zhang, Z., Louie, S. & Chan, C. T. Klein tunneling and supercollimation of pseudospin-1 electromagnetic waves. *Phys. Rev. B* **93**, 035422 (2016).

34. Mei, J., Ying, W., Chan, C. T. & Zhang, Z. Q. First-principles study of Dirac and Dirac-like cones in phononic and photonic crystals. *Phys. Rev. B* **86**, 035141 (2012).

35. Huang, X., Lai, Y., Hang, Z. H., Zheng, H. & Chan, C. T. Dirac cones induced by accidental degeneracy in photonic crystals and zero-refractive-index materials. *Nat. Mater.* **10**, 582–586 (2011).

36. Xing, G. et al. Low-temperature solution-processed wavelength-tunable perovskites for lasing. *Nat. Mater.* **13**, 476–480 (2014).

37. Zhang, Q., Ha, S. T., Liu, X., Sum, T. C. & Xiong, Q. Room-temperature near-infrared high-*Q* perovskite whispering-gallery planar nanolasers. *Nano Lett.* **14**, 5995–6001 (2014).

38. Zhu, H. et al. Lead halide perovskite nanowire lasers with low lasing thresholds and high quality factors. *Nat. Mater.* **14**, 636–642 (2015).

39. Su, R. et al. Perovskite semiconductors for room-temperature exciton-polaritonics. *Nat. Mater.* **20**, 1315–1324 (2021).

40. Su, R. et al. Observation of exciton polariton condensation in a perovskite lattice at room temperature. *Nat. Phys.* **16**, 301–306 (2020).

41. Ghosh, S. et al. Microcavity exciton polaritons at room temperature. *Photon. Insights* **1**, R04 (2022).

Methods

Numerical simulations

In this work, all the simulations are conducted by the finite element method solver in COMSOL Multiphysics. Bloch boundary conditions are employed in the x and y directions, whereas perfectly matched layers are utilized in the z direction. The refractive indices of perovskites and the environment are set as 2.25 and 1.50, respectively.

Optical characterization

The photonic band structures and emission of perovskite metasurfaces are measured by angle-resolved PL spectroscopy with a Fourier imaging configuration. The PL signals are collected by a ×50 microscope objective with a numerical aperture of 0.75. PL dispersion, lasing emission and k-space images are detected by an imaging spectroscope (HORIBA, iHR550) having 600 gratings mm^{-1} and a liquid-nitrogen-cooled charge-coupled device. The polarization of emission is resolved by a polarizer and a quarter-wave plate. The perovskite metasurface is excited by a 455 nm continuous-wave laser for PL emission, whereas it is pumped at 400 nm by using a Ti:sapphire femtosecond laser (100 fs pulse duration and 1 kHz repetition rate) for lasing. The zoomed-in momentum-space images are measured by magnifying the $k_\parallel = 0$ region with a couple of lenses, namely, f_1:$f_2 = 1$:5, where f_1 and f_2 are the focal length of the two lenses.

Data availability

The data that support the plots within this paper and other findings of this study are available from the corresponding authors upon reasonable request. The raw data are available via the repository at https://figshare.com/articles/dataset/Raw_data_for_NM22061931A/22226455.

Author contributions

Y.C., Q.X. and C.-W.Q. conceived the idea. Y.C. designed the metasurfaces and conducted the simulations, and J.F. designed the experiments. J.F. and Q.X. oversaw and conducted the nanofabrication, perovskite assembly and optical spectroscopy measurements. Y. Huang developed the theoretical model and analysis. R.S. and Y. Hou provided support on sample synthesis and optical measurements. W.C. and S.G. provided support on simulation. Y.C. and J.F. analysed the data. Y.C., J.F., Y. Huang, Q.X. and C.-W.Q. drafted the paper with inputs from all the authors. Q.X. and C.-W.Q. supervised the project.

Competing interests

The authors declare no competing interests.

Additional information

Supplementary information The online version contains supplementary material available at https://doi.org/10.1038/s41563-023-01531-2.

Correspondence and requests for materials should be addressed to Jiangang Feng, Qihua Xiong or Cheng-Wei Qiu.

Peer review information *Nature Materials* thanks Makhsud Saidaminov and the other, anonymous, reviewer(s) for their contribution to the peer review of this work.

Reprints and permissions information is available at www.nature.com/reprints.